

## ELECTROCHEMICAL SCIENCE AND TECHNOLOGY

## Simulation and Optimization of the Dual Lithium Ion Insertion Cell

Thomas F. Fuller,\* Marc Doyle,\* and John Newman\*\*

Department of Chemical Engineering, University of California, and  
Materials Sciences Division, Lawrence Berkeley Laboratory, Berkeley, California 94720

## ABSTRACT

The galvanostatic charge and discharge of a dual lithium ion insertion (rocking-chair) cell are modeled. Transport in the electrolyte is described with concentrated solution theory. Insertion of lithium into and out of the active electrode material is simulated using superposition, greatly simplifying the numerical calculations. Simulation results are presented for the  $\text{Li}_x\text{C}_6$ /propylene carbonate +1M  $\text{LiClO}_4$ / $\text{Li}_x\text{Mn}_2\text{O}_4$  cell, and these results are compared with experimental data from the literature. Criteria are established to assess the importance of diffusion in the solid matrix and of transport in the electrolytic solution. Various procedures to optimize the utilization of active material are considered. Simulation results for the dual lithium ion insertion cell are compared with those for a cell with a solid lithium negative electrode.

The storage and conversion of energy continues to be important to society. Batteries, which interconvert chemical and electrical energy, are widely used in industry and for consumer applications (e.g., appliances and laptop computers). At the same time, environmental concerns are reshaping many industries. The ecological hazards of batteries through their operation and disposal is a primary consideration for battery manufacturers. In addition, stricter emission standards on automobiles are spurring interest in batteries for electric-vehicle applications. The energy and power requirements for vehicle propulsion are rigorous.<sup>1</sup> Consequently, research on rechargeable battery systems is receiving renewed attention.

Lithium batteries are attractive for energy storage because of their high theoretical energy densities. Furthermore, they are less toxic than nickel cadmium or lead acid cells, and their disposal poses fewer environmental problems. Although primary lithium batteries have been mass-produced for years,<sup>2</sup> the secondary (rechargeable) lithium cell has been commercialized only recently.<sup>3-5</sup> The typical lithium cell is made up of a lithium metal negative electrode, an electrolyte which serves as an ionic path between electrodes and separates the two materials, and a positive electrode, such as  $\text{Mn}_2\text{O}_4$ .

In general, a highly reactive material is desired for the negative electrode to give a higher cell potential, and hence a higher theoretical energy density. Unfortunately, the more reactive the electrode material the more likely it reacts irreversibly with the electrolyte. The high reactivity of lithium metal is a significant problem for lithium batteries. Successful lithium battery systems operate due to a protective film that forms on the electrode surface.<sup>6</sup> This protective film retards further reaction with the electrolyte but impacts the capacity and cycle life of the cell through increased resistance and material isolation. The highly reactive lithium metal is a safety issue as well, becoming especially important in larger cells.

One alternative scheme has been to replace the lithium metal negative electrode with a lithium alloy or compound, such as:  $\text{LiAl}$ ,<sup>7</sup>  $\text{LiFe}_2\text{O}_3$ ,<sup>8</sup>  $\text{LiWO}_2$ ,<sup>9</sup> or  $\text{LiC}_6$ .<sup>9</sup> Although these materials stabilize the lithium, this reduces the energy density of the cell, since the added material is not used in the

operation of the system. Even with this drawback, several lithium batteries have been developed using this strategy.

Rechargeable batteries for electric-vehicle applications require long cycle life; 500 to 1000 cycles is desired before the capacity falls below 80% of its initial value. For this to be possible, the electrochemical reactions must be highly reversible. Some of the most reversible electrodes operate through insertion reactions. In these electrodes, commonly layered transition metal oxides, the ionic species is transported across the electrolyte and diffuses between the layers or in interstitial sites of the electrode structure where it is stabilized by favorable coulombic interactions. Because there is no bond breaking or appreciable restructuring of the electrode during this process, the mechanism is highly reversible. A general discussion of the insertion process has been given by Whittingham.<sup>10,11</sup> Hundreds of materials that insert lithium ions reversibly have been developed and tested since their usefulness for battery applications was recognized.<sup>12</sup>

Some years ago it was realized that replacing the lithium metal with another insertion material was a possible solution to the high reactivity and irreversibilities of the solid lithium negative electrode.<sup>13</sup> This material must insert lithium at a potential that is appreciably lower than that of the positive electrode; in effect, it must have less favorable energetics for the insertion process. The cell potential results from differences in the activity of lithium in the two insertion materials. The operation of the system then involves the shuttling of lithium ions back and forth between the two insertion compounds, and hence sometimes has been given the colloquial name rocking-chair cell.<sup>14</sup> These systems have a lower energy density than those with solid lithium as discussed above. The reversibility and improved safety of these systems make them attractive nonetheless. Several companies recently have announced their intentions to bring rechargeable batteries based on this concept to market.<sup>4,5</sup> More background on the conceptual development of the dual insertion battery is given by Scrosati.<sup>15</sup>

The development of a detailed mathematical model is important to the design and optimization of lithium secondary cells and critical in their scale-up. West *et al.*<sup>16</sup> treated insertion into a composite cathode consisting of an active insertion material and electrolyte in a porous structure, but did not consider a full cell. A more complete model

\* Electrochemical Society Student Member.

\*\* Electrochemical Society Active Member.

of a lithium-anode, solid-polymer-electrolyte, porous-insertion-cathode cell was given by Doyle *et al.*<sup>17</sup> Simulation results for a lithium metal anode, polyethylene oxide separator, and  $\text{TiS}_2$  composite cathode, including discharge curves and concentration profiles, are provided.

Our objective here is to develop a general model of the dual insertion cell. Given the physical properties and system parameters, the model can simulate any particular choice of materials. This model is used to evaluate the performance of a specific system, and the simulation results are compared with experimental discharge curves obtained from the literature. In particular, we can assess the importance of diffusion in the solid material, which is thought to be a limitation in some cells. Different applications may require different rates of discharge. This model allows us to evaluate the suitability of various systems for these applications. Finally, the optimization of the performance of these cells is discussed.

### Model Development

We have modeled the galvanostatic charge and discharge of the cell sandwich shown in Fig. 1. We consider one-dimensional transport of lithium ions from the negative electrode through the separator into the positive electrode. The composite electrodes consist of an inert conducting material, the electrolyte, and the solid active insertion particles. The theory derives from work of Newman<sup>18</sup> and from the preceding model of Doyle *et al.*<sup>17</sup> Consequently, only the salient features of the model are given here. We focus instead on the discussion of simulation results and optimization issues.

Transport in the separator is modeled with concentrated solution theory, assuming a binary electrolyte and solvent. With three species (*e.g.*,  $\text{Li}^+$ ,  $\text{X}^-$ , and solvent), the electrical conductivity, the transference number of the lithium ion, and the diffusion coefficient of the lithium salt characterize transport in the electrolyte. This macroscopic approach, using concentrated solution theory with variable physical properties, allows one to deal rigorously with the transport phenomena.

In concentrated solution theory, the driving force for mass transfer is the gradient in electrochemical potential

$$c_i \nabla \mu_i = \sum_{j \neq i} K_{ij} (v_j - v_i) \quad [1]$$

where the  $K_{ij}$  ( $K_{ij} = K_{ji}$ ) are frictional coefficients describing interactions between species *i* and *j*. For a solution of a binary salt plus solvent, because of the Gibbs-Duhem equation, we have two independent transport equations of the form given in Eq. 1. If we use the solvent as the reference species and take its velocity to be zero, we can invert these equations to obtain

$$\mathbf{N}_+ = -v_+ D \nabla c + \frac{i t_+^0}{z_+ F} \quad [2]$$

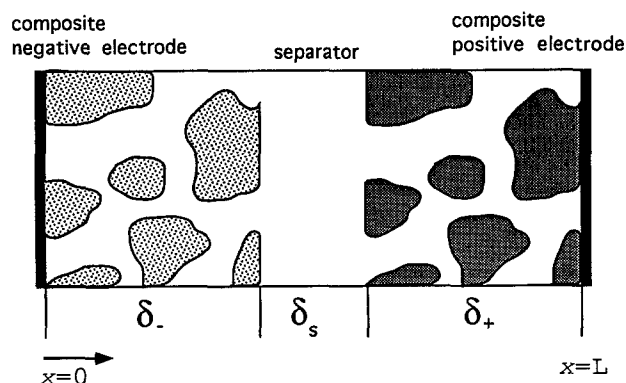


Fig. 1. Dual-insertion cell sandwich consisting of composite negative and positive electrodes and separator.

and

$$\mathbf{N}_- = -v_- D \nabla c + \frac{i t_-^0}{z_- F} \quad [3]$$

*c* is the concentration of the electrolyte ( $c = c_i/v_i$ ). The  $K_{ij}$ 's can be related directly to the three measurable transport properties  $D$ ,  $t_+^0$ , and  $\kappa$ .<sup>17-19</sup>

A material balance on the electrolyte gives

$$\epsilon \frac{\partial c}{\partial t} = \nabla \cdot (\epsilon D \nabla c) - \frac{j_2 \cdot \nabla t_+^0}{z_+ v_+ F} + \frac{a j_n (1 - t_+^0)}{v_+} \quad [4]$$

where  $\epsilon$  is the volume fraction of the electrolyte. We have assumed that the porosity is constant and that volume changes can be neglected.  $j_n$  is the pore-wall flux across the interface between the electrolyte and the active material. This pore-wall flux is averaged over the interfacial area between the solid matrix and the electrolyte. Thus, the last term can be viewed as a reaction rate per unit volume, and Eq. 4 is analogous to the treatment of a packed-bed reactor.

The current density in the two phases is conserved

$$I = i_1 + i_2 \quad [5]$$

The total current density, *I*, is uniform and flows through either the electrolyte phase ( $i_2$ ) or through the insertion material phase ( $i_1$ ). The current flowing in the matrix is governed by Ohm's law

$$i_1 = -\sigma \nabla \Phi_1 \quad [6]$$

The variation of potential in the electrolyte is<sup>18</sup>

$$i_2 = -\kappa \nabla \Phi_2 + \frac{\kappa RT}{F} \left( 1 + \frac{\partial \ln f_A}{\partial \ln c} \right) (1 - t_+^0) \nabla \ln c \quad [7]$$

where  $\Phi_2$  is measured with a lithium reference electrode in solution. Equation 7 is similar to Ohm's law but includes a term for concentration variations. The pore-wall flux,  $j_n$ , is related to the divergence of the current flow in the electrolyte phase through Faraday's law

$$a j_n = \frac{-s_i}{nF} \nabla \cdot i_2 \quad [8]$$

Boundary conditions for Eq. 4, 6, and 7 derive from the condition that the flux density of each ionic species must be zero at the ends of the cell. From this, we obtain the conditions that

$$\nabla c = 0 \text{ at } x = 0 \text{ and } x = L$$

At the ends of the cell, we also can say that the current flows in the solid matrix only ( $i_2 = 0$ ). Thus from Eq. 5 and 6, we find

$$\nabla \Phi_1 = -I/\sigma \text{ at } x = 0 \text{ and } x = L \quad [9]$$

Because we are interested only in potential differences, we arbitrarily set the potential in the solution phase to zero at  $x = L$ ; for galvanostatic behavior, we specify the current ( $I = i_2$ ) in the separator.

In porous media, transport properties must be modified to account for the actual path length of the species.<sup>20</sup> Therefore in the composite electrodes

$$\kappa_{\text{eff}} = \kappa \epsilon^{1.5}$$

and

$$D_{\text{eff}} = D \epsilon^{0.5}$$

The active electrode material is assumed to be made up of spherical particles of radius  $R_s$  with diffusion being the mechanism of transport of the lithium into the particle. The model can also simulate cylindrical and planar particles of given size; the treatment is analogous. We take the direction normal to the surface of the particles to be the *r*-direction. Thus

$$\frac{\partial c_s}{\partial t} = D_s \left[ \frac{\partial^2 c_s}{\partial r^2} + \frac{2}{r} \frac{\partial c_s}{\partial r} \right] \quad [10]$$

where  $c_s$  represents the concentration of lithium in the solid particle phase. From symmetry

$$\frac{\partial c_s}{\partial r} = 0 \text{ at } r = 0 \quad [11]$$

The second boundary condition is provided by a relationship between the pore-wall flux across the interface and the rate of diffusion of lithium ions into the surface of the insertion material

$$j_n = -D_s \frac{\partial c_s}{\partial r} \text{ at } r = R_s \quad [12]$$

As the diffusion coefficient of the inserted lithium ions has been assumed constant, this is a linear problem and can be solved by the method of superposition<sup>21</sup> (Appendix B). In brief, we can calculate the flux at the surface of the insertion particles from the prior surface concentrations and a series of coefficients which are calculated separately.

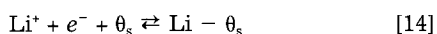
The open-circuit potential of insertion materials varies with the amount of lithium inserted and is expressed by a general function of composition in the particle

$$U = U^0 - U_{\text{ref}}^0 + F(c_s) \quad [13]$$

The function  $F(c_s)$  can vary widely depending on the insertion chemistry of the material. For example, lithium inserts into  $\text{TiS}_2$  between layers of sulfur atoms, held together by weak van der Waals forces, forming a continuous phase that is saltlike. There is a small change in free energy with the amount of lithium inserted, and the cell potential decreases slowly with lithium content. Insertion into manganese dioxide causes a distortion in the crystal lattice. This electrode has an open-circuit potential that exhibits two plateaus corresponding to the thermodynamic potentials of each phase transition. By definition, compounds such as the manganese dioxide that exhibit phase changes during discharge are not true insertion materials, as insertion is a nonstoichiometric process that should not involve formation of a specific phase. However, for this model even compounds that have phase changes are treated as insertion materials. Our model is general and any continuous function can be used for the open-circuit potential above.

There are limited data available on the kinetics of the charge-transfer reaction at the surface of insertion compounds. Pollard and Newman<sup>22</sup> have shown that the assumption of infinitely fast kinetics for a porous electrode leads to a spike in the local current density at the separator/electrode interface at short times. Assuming infinitely fast kinetics also changes the governing equations. We wish to keep the model general so that the kinetics of the electrodes can be included if data are available. Consequently, a charge-transfer resistance is considered in the present model. Due to a lack of data, the values used for the exchange current densities at the insertion material surfaces correspond to highly reversible charge-transfer processes.

For a general charge-transfer reaction from a liquid electrolyte, the following form is assumed for the insertion process



Here  $\theta_s$  represents a site in the solid insertion material. If the kinetics follow a Butler-Volmer form<sup>a</sup>

$$j_n = k(c)^{\alpha_a}(c_t - c_s)^{\alpha_a}(c_s)^{\alpha_c} \left\{ \exp\left(\frac{\alpha_a F}{RT}(\eta - U)\right) - \exp\left(-\frac{\alpha_c F}{RT}(\eta - U)\right) \right\} \quad [15]$$

Here  $k$  represents the product of the forward and backward rate constants, each raised to a power depending on the transfer coefficients, for the charge-transfer reaction at the electrode surface. The overpotential  $\eta$  is defined as

$$\eta = \Phi_1 - \Phi_2 \quad [16]$$

Equations 4, 6, 7, 8, 10, and 12 are linearized and solved simultaneously using the subroutine BAND.<sup>18</sup> We have two independent variables ( $x$  and  $t$ ) and six dependent vari-

<sup>a</sup> For the carbon electrode 0.5c<sub>i</sub> was used in place of c<sub>i</sub> due to the limited cycling regime of this material.

Table I. Parameters for the electrodes.

Parameter	Li <sub>y</sub> Mn <sub>2</sub> O <sub>4</sub>	Li <sub>x</sub> C <sub>6</sub>
$D_s$ (cm <sup>2</sup> /s)	$10^{-9.22}$	$5.0 \times 10^{-9.22}$
$\sigma$ (S/cm)	1.0	1.0
$i_0$ (mA/cm <sup>2</sup> )	0.289 <sup>a</sup>	0.041 <sup>a</sup>
$\alpha_a, \alpha_c$	0.5	0.5
$c_i$ (mol/dm <sup>3</sup> )	23.72	26.40
$\rho_s$ (g/cm <sup>3</sup> )	4.1	1.9

<sup>a</sup> Assumed value at initial conditions.

ables ( $c$ ,  $\Phi_2$ ,  $c_s$ ,  $i_2$ ,  $j_n$  and  $\Phi_1$ ). The Crank-Nicolson implicit method was used to evaluate the time derivatives.

## Results and Discussion

Appendix A gives transport properties for the electrolyte and thermodynamic data for each electrode. We modeled a cell consisting of a carbon negative electrode, lithium perchlorate in a propylene carbonate liquid electrolyte, and manganese dioxide positive electrode. The lithium perchlorate/propylene carbonate electrolyte in the separator region of the cell was assumed to be confined to the voids of an inert polymer material such as polypropylene. The inert separating material is assumed to have a constant void fraction of 0.4, and transport properties of the electrolyte in this region are adjusted accordingly. The carbon material was petroleum coke, with the composition range for lithium insertion being  $0 < x < 0.5$ , that used by Guyomard and Tarascon.<sup>23</sup>

The optimum solvent for this system is not propylene carbonate alone, but rather a mixed solvent system. These solvent mixtures allow a more reversible insertion process at the carbon electrode<sup>9</sup> and exhibit better conductivities.<sup>24</sup> However, reliable values of the lithium ion transference number and salt diffusion coefficient do not exist for these systems. We simulated propylene carbonate alone because the transport properties for this solvent are known. Even for lithium perchlorate in propylene carbonate, the variations of the transport properties with concentration are incomplete. For this reason, the concentration dependence of the conductivity is the only variable physical property included in these simulations.

Additional parameters used in this model are listed in Tables I and II. The quantities in Table I are inherent properties of the specific system and can be determined from experimental measurement. Quantities in Table II can be varied to optimize a particular battery design. These adjustable parameters, where possible, have been chosen to correspond to those used by Guyomard and Tarascon,<sup>23</sup> permitting a comparison with their experimental results.

The moderately high electronic conductivity used for the two electrodes is that obtained with a small fraction of conducting material (carbon black) added to the solid matrix. We did not consider the effects of low electronic conductivity on the discharge behavior as this is an unnecessary complication that is avoided in practical systems. The volume fraction of conducting filler added to each electrode was chosen to correspond to that used by Guyomard and Tarascon.<sup>23</sup> The maximum concentrations in the positive and negative electrodes are estimated from the density

Table II. Design adjustable parameters.

Parameter	Li <sub>y</sub> Mn <sub>2</sub> O <sub>4</sub>	Li <sub>x</sub> C <sub>6</sub>
$\delta_+$ , $\delta_-$ (μm)	200	243
$R_s$ (μm)	1	18
$c_s^0$ (mol/dm <sup>3</sup> )	4.744	13.07
$\epsilon$	0.3	0.3
$\epsilon_f$	0.151	0.044
Parameter	Value	
$T$ (°C)	25	
$c^0$ (mol/dm <sup>3</sup> )	1.00	
$\delta_s$ (μm)	50	
$z$	0.62	



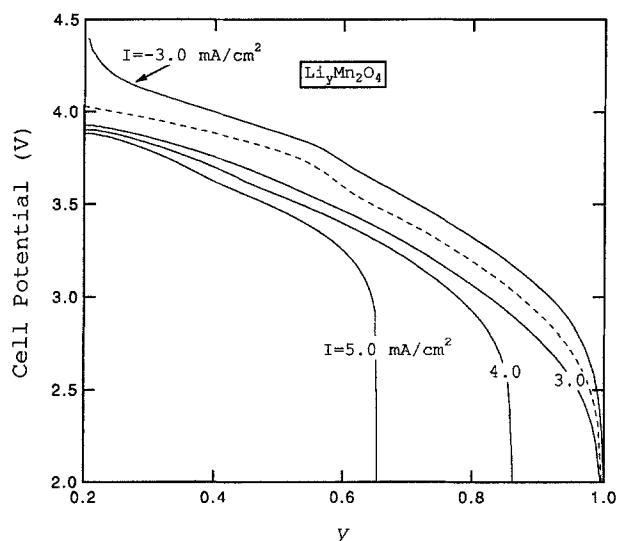


Fig. 2. Cell potential vs. state of discharge for the manganese dioxide/carbon system at various discharge rates. The dashed line is the open-circuit potential of the cell. Other parameters used in the simulation are given in Tables I and II.

and molecular weight of the material at composition  $\text{LiMn}_2\text{O}_4$  or  $\text{LiC}_6$ , respectively.  $z$  is the capacity ratio of the positive to negative electrode

$$z = \frac{c_{t+}(1 - \epsilon_+ - \epsilon_{t+})\delta_+}{c_{t-}(1 - \epsilon_- - \epsilon_{t-})\delta_-} \quad [17]$$

Figure 2 shows the cell potential as a function of utilization of positive electrode material for galvanostatic charge and discharge for the carbon/manganese dioxide cell. The state of charge is measured with  $y$ , the stoichiometry of the positive electrode. The manganese dioxide electrode is assumed to insert lithium over the range ( $0.2 < y < 1.0$ ); hence, the initial solid concentration is 20% of the total, or maximum, concentration. For this system, during charge,  $y$  varies between 1 and 0.2, and  $x$  varies between 0 and 0.495.  $x$  and  $y$  are related through the capacity ratio  $z$

$$z = \frac{\Delta x}{\Delta y} \quad [18]$$

The dashed line represents the open-circuit potential calculated from equations in Appendix A, and the current density is a parameter.

The cell potential for this system during discharge at  $4.0 \text{ mA/cm}^2$  is predicted to be approximately  $3.89 \text{ V}$  at the start of discharge and decreases to about  $2.90 \text{ V}$  at  $y = 0.8$ . This is the same range exhibited by cells discharged by Guyomard and Tarascon.<sup>23</sup> At higher current densities, ohmic losses are larger, and the cell potential is lower irrespective of concentration polarization. It is apparent that the material utilization is limited at higher discharge rates. For this system, the abrupt drop in cell potential at the higher discharge rates is caused by concentration polarization as is discussed further below. We show that at current densities above ca.  $4.0 \text{ mA/cm}^2$  the utilization of active material begins to drop off for this particular system. This discharge rate is comparable to that obtained by Guyomard and Tarascon<sup>23</sup> for manganese dioxide systems of similar thicknesses (see Fig. 17 of the cited reference). The above authors were not using a porous electrode, so their system should sustain lower rates of discharge (because of solid-state diffusion).

The concentration of the electrolyte over the time scale of a full discharge is depicted in Fig. 3 for a current of  $4.0 \text{ mA/cm}^2$ . Initially the concentration is uniform at  $1.00 \text{ mol/dm}^3$ . Li deinserts from the carbon electrode and inserts into the manganese dioxide electrode on discharge. Since the perchlorate anions are not involved in the electrochemical reactions, their flux is zero at steady state. A concentration

gradient builds up to balance the migration of anions. This gradient is seen clearly from Eq. 3. The concentration profile is established quickly in comparison to the time of discharge. Near the end of discharge (65 min), the concentration of the electrolyte at the back of the manganese dioxide electrode is driven to zero, a limiting-current phenomenon. Once this happens, the active manganese dioxide material in this region can no longer be used because there are no lithium ions in the solution phase to insert. At higher current densities, the electrolyte concentration is driven to zero closer to the separator, thus preventing 100% utilization of the electrode. At current densities lower than  $3.0 \text{ mA/cm}^2$ , a limiting current is never reached.

An important factor in optimizing the performance of the cell is good utilization of the active material. For a specified battery performance, the cell potential should fall below its cutoff value only after nearly all the active material is consumed. This result requires an understanding of the transport limitations in each phase of the composite electrodes, as these lead to nonuniform reaction distributions.

The importance of diffusion in the solid electrode material can be assessed from the dimensionless parameter  $S_s$

$$S_s = \frac{R_s I}{D_s n F (1 - \epsilon - \epsilon_{t+})(c_t - c_s^0)\delta_+} \quad [19]$$

and is the ratio of diffusion time in either electrode to the discharge time for the positive electrode. Here the discharge time is calculated based on the maximum concentration in the solid and the range of  $y$  during cycling. If the positive electrode is not limiting, Eq. 19 can be modified to reflect the time of discharge. For  $S_s \ll 1$ , diffusion in the solid can be neglected. For the dual insertion systems, there is a different value of this parameter for each electrode. Substitution of the parameters from Table I into Eq. 19 with  $I = 4.0 \text{ mA/cm}^2$  gives  $S \approx 0.002$  for the manganese dioxide electrode and  $S \approx 0.129$  for the carbon electrode. Thus, diffusion limitations are not expected to exist in the manganese dioxide particles, but they may exist in the carbon. Therefore, for the manganese dioxide particles the concentration at the surface and the average concentration in the solid are nearly identical, and we do not present concentration profiles in the solid.

A typical concentration profile in a solid carbon particle is presented in Fig. 4. This particle is located near the carbon electrode/separator boundary ( $\bar{x} = 0.4$ ), and the profile is taken close to the end of discharge. Since the shape of the profiles does not change significantly over the course of discharge for this simulation, this profile is a good representation of the extent of diffusion limitations in the solid

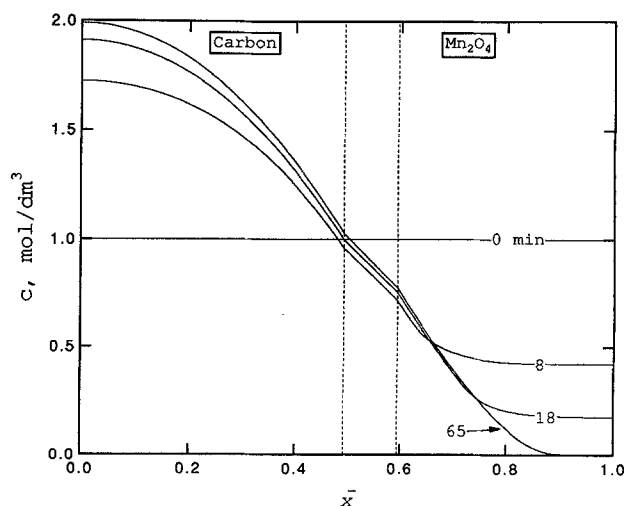


Fig. 3. Concentration profiles across the cell during galvanostatic discharge at  $I = 4.0 \text{ mA/cm}^2$ . Carbon negative electrode is 21.5% thicker than the manganese dioxide positive electrode. The separator region is set off by the dashed lines.

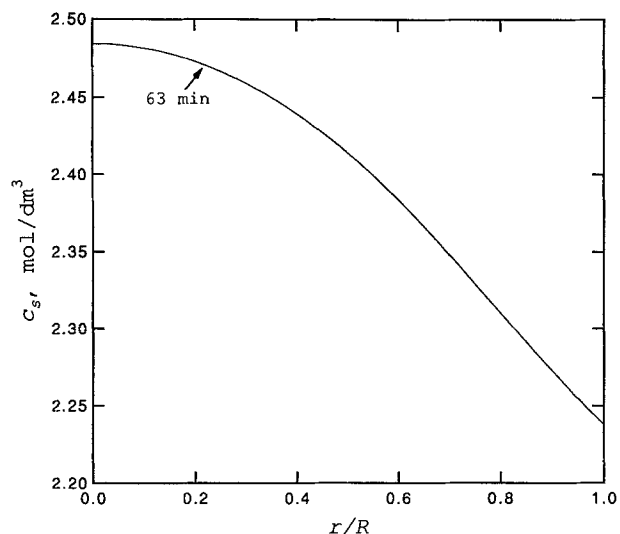


Fig. 4. Concentration of lithium inside a solid carbon particle. The discharge rate is  $i = 4.0 \text{ mA/cm}^2$ , and the time since the beginning of discharge is 63 min. The particle is located at  $\bar{x} = 0.4$ , near the negative electrode/separator boundary.

particles. The concentration difference inside the carbon particles is fairly small, about 10% of the average concentration in the particle. This result is in good agreement with the value of  $S_s$  calculated above for the carbon particles.

We can use  $S_s$  to predict the radius of the particles for which severe diffusion limitations exist in the solid phase for this system. We find that diffusion limitations begin, i.e.,  $S_s = 1$ , when the manganese dioxide particle radius exceeds  $24 \text{ }\mu\text{m}$ . This result is especially relevant to non-porous electrode structures, where the solid-phase diffusion length is often on this order. Calculating the value of  $S_s$  for the nonporous manganese dioxide electrode (thickness of  $170 \text{ }\mu\text{m}$ ) used in Guyomard and Tarascon's<sup>23</sup> work, one finds that  $S = 37$ . As  $S > 1$ , we expect that this is the main factor limiting the utilization of material at high rates of discharge in their system.

An analogous parameter can be calculated relating the time constant for transport of the electrolyte to the time of the discharge

$$S_e = \frac{L^2 I}{DnF(1 - \epsilon - \epsilon_{t,e})(c_t - c_s^0)\delta_s} \quad [20]$$

For  $I = 4.0 \text{ mA/cm}^2$ , we find that  $S_e = 0.187$ . This relatively low value explains why the concentration profile in Fig. 3 is established quickly compared to the discharge time. Because the time for transport in the electrolyte may be small in comparison to the discharge time, a quasi-steady-state concentration profile is established.

Transport limitations in the electrolyte phase are the main factor limiting the performance of this cell at high discharge rates. The mechanism of failure is the depletion of the electrolyte in the solution phase, which leads to a large concentration overpotential. This result is less of a problem with larger values of the salt diffusion coefficient, the initial salt concentration, or the lithium ion transference number. At higher discharge rates, the concentration in the solution phase can be driven to zero well before 100% utilization has been attained, leading therefore to incomplete utilization of the active material.

As this is the major cause of the end of discharge, it suggests that increasing the electrolyte concentration would improve the performance of the system at high rates of discharge. The value of the initial concentration used in these systems is generally chosen to correspond to a conductivity maximum. This correspondence can be seen for the present system in the figures given in Ref. 23, where the concentration dependence of the conductivity for this system was obtained. Thus, increasing the concentration above this maximum leads to an increase in the ohmic drop

in the system. However, as has been stressed before,<sup>17</sup> the advantages in terms of the increased concentration in the depth of the porous electrode generally outweigh the increase in ohmic drop. This advantage can be demonstrated by simulating the system at a high rate of discharge corresponding to  $I = 5.0 \text{ mA/cm}^2$  with the initial concentration as a parameter. The results, in the form of discharge curves, are presented in Fig. 5. Even a small increase in the initial concentration brings about a marked improvement in the attainable utilization. When the initial concentration is increased by 40%, almost complete utilization is obtained.

Raising the initial concentration leads to much higher concentrations in the negative electrode on discharge, which may cause problems in lithium salt/solvent systems that have a solubility limit. The maximum concentration attained by the system can be checked using the current model to ensure that a solubility limit is not surpassed. For instance, the solubility limit of lithium perchlorate in propylene carbonate at room temperature is  $2 \cdot 10 \text{ mol/dm}^3$ .<sup>23</sup> Concentrations above this are obtained in the negative electrode for current densities greater than  $5.0 \text{ mA/cm}^2$ . This model does not account for salt precipitation, but this is an undesirable situation that should be avoided in practice. For the present system, the concentration dependence of the conductivity, but not the transference number and diffusion coefficient, is included (Appendix A). To model correctly the possible benefits of increasing the initial concentration in the system further, all these concentration dependences should be included, as well as a consideration of solubility limitations.

Figure 6 shows the divergence of the solution-phase current, which is proportional to the reaction rate per unit volume, across the cathode at various times during discharge. This figure is analogous to a current distribution on the surface of an electrode. The shape of the curves is complex in general, depending on ohmic resistance, electrode kinetics, open-circuit potential, and any transport limitations that exist. Newman<sup>18</sup> gives four dimensionless parameters that characterize the current distribution in a porous electrode. These parameters describe the balance between ohmic and kinetic limitations, but not concentration effects. At short times, the concentration of electrolyte is nearly constant, and these parameters can be used to describe the current distribution. An analysis of this sort has been carried out in an earlier paper<sup>17</sup> and will not be repeated here.

Predicting the current distribution at long times is more difficult. Not only does the depletion of the electrolyte

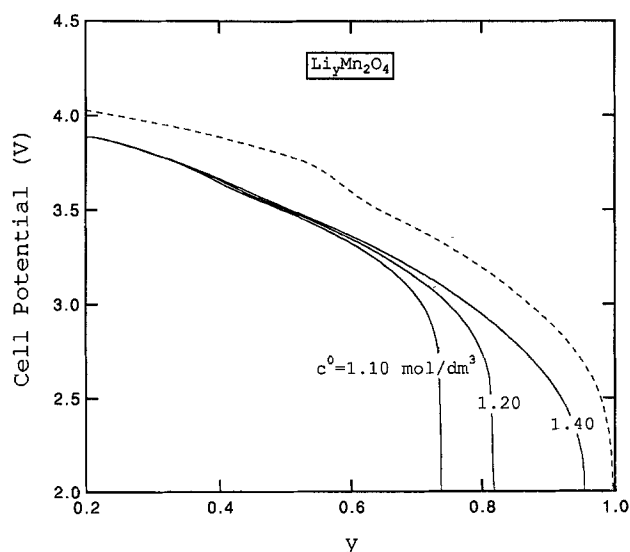


Fig. 5. Cell potential vs. state of discharge for the manganese dioxide/carbon system with the initial electrolyte concentration as a parameter. The dashed line is the open-circuit potential of the cell. The discharge rate is  $I = 5.0 \text{ mA/cm}^2$ .

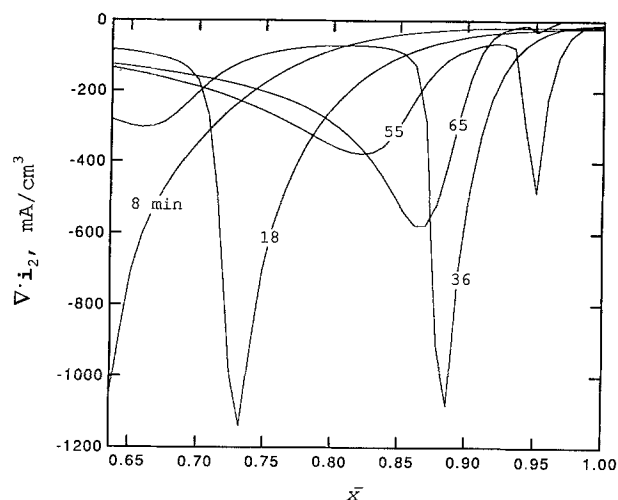


Fig. 6. Divergence of the solution-phase current density, which is proportional to the pore wall flux of lithium into the positive-electrode active material, during galvanostatic discharge at  $i = 4.0 \text{ mA/cm}^2$ . Time since the beginning of discharge is given in minutes.

cause concentration polarization to occur, but also it affects the kinetic expression and the transport properties. In addition, in insertion systems, the dependence of the open-circuit potential on the state of charge has an appreciable effect on the current distribution. This effect has been observed in other systems with a similar dependence of open-circuit potential on concentration. A strong dependence of open-circuit potential on concentration causes a more nearly uniform current distribution. This is analogous to the effect of the kinetic resistance on the current distribution. In contrast, systems like manganese dioxide, which exhibit a flat open-circuit potential, tend to have nonuniform current distributions, often resulting in a spike-shaped reaction front moving through the electrode.

With this in mind, we can explain some of the general features of Fig. 6. The open-circuit potential *vs.* state of charge for the carbon and manganese dioxide materials used here is given for reference as Fig. A-1 and A-2. Initially ( $t = 8 \text{ min}$ ), we have the distribution skewed toward the front of the electrode, characteristic of an ohmically dominated system with the ionic conductivity of the solution much lower than the electronic conductivity of the solid phase. Then, as the active material at the front of the electrode becomes exhausted, a spike of current develops and moves across the electrode. This spike reaches the back face of the electrode when the overall utilization is about 60%, which corresponds to the end of a flat section on the open-circuit potential curve for manganese dioxide. After this, the distribution is briefly more uniform, as the open-circuit potential becomes more sloped with state of charge in this region. Then, as the open-circuit potential again levels off, another smaller spike develops and moves across the electrode consuming the remaining active material. The end of the first reaction spike and the beginning of the second spike can be seen clearly on the  $t = 36 \text{ min}$  curve of Fig. 6. A similar current distribution, involving two successive spikes moving through the porous electrode, has been predicted for the LiAl/FeS cell.<sup>7</sup> There are two possible positive-electrode reactions in the iron sulfide electrode, having slightly displaced open-circuit potentials.

The current distribution in the carbon electrode is not presented because it quickly becomes uniform. Initially it also is skewed toward the front of the electrode, representing the dominance of ohmic effects. At later times the distribution is uniform, which agrees with the analysis above because the open-circuit potential of carbon is strongly dependent on the state of charge. The current distributions are similar to those seen in the titanium disulfide electrode,<sup>17</sup> which has a similar dependence of open-circuit potential on state of charge.

Figure 7 shows the local utilization ( $y$  or  $x$ ), which is proportional to the average concentration of lithium in the solid phase of each electrode. This figure allows one to examine the relationship between electrode thickness and active-material utilization. Local utilization in the carbon electrode is nearly uniform. This was supported earlier by the discussion of the current distribution in this electrode. In contrast, the local utilization in the manganese dioxide electrode is complex. This is a result of the general shape of the open-circuit potential function and also extreme concentration polarization in the electrolyte. Much of the analysis on Fig. 6 for the current distribution in the manganese dioxide electrode can be reexamined and confirmed using this figure. It is apparent from this figure that the material near the back face of the positive electrode is not fully utilized in this system.

Finally, we examine the power and energy density for the carbon/manganese dioxide system. These densities are based on the mass of both composite electrodes and the separator, but not on other battery components such as current collectors, terminals, and casing. Densities of the active materials used in these simulations are given in Table I. The density of the electronically conducting filler and inert separator materials are both taken to be  $2.0 \text{ g/cm}^3$ . The mass per unit area for each curve can be calculated from the densities and system parameters. Figures 8 and 9 (Ragone-type plots) show the effect of electrode thickness and porosity on the performance of the system. The power provided here is an average value over the course of discharge. Thus, each point on these figures is obtained by carrying out a constant-current discharge at a particular discharge rate to a cutoff potential of  $2.0 \text{ V}$  and calculating the energy and the average power available during the discharge. At low current densities, the energy density approaches a theoretical limit, which is a function of the open-circuit potential. Lines representing several constant discharge times also are shown on these figures. Three hours correspond to the usual time for discharge of electric-vehicle batteries.

First, we consider the effect of electrode thickness on the performance of the system. The capacity ratio for the two electrodes was kept constant here; thus, as the thickness of the positive electrode is varied, the negative electrode is always 1.21 times thicker. The porosities of the two electrodes are kept constant and equal to the values used in the preceding simulations. Figure 8 exhibits the usual tradeoff between power and energy densities when thickness is varied. For thin electrodes a large power density is attainable, but the maximum energy density suffers as the mass of the separator becomes an appreciable fraction of the

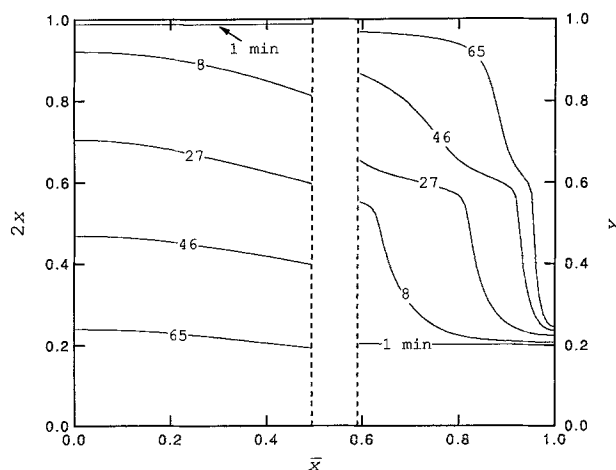


Fig. 7. Local utilization of active material across the full cell during galvanostatic discharge at  $i = 4.0 \text{ mA/cm}^2$  for the carbon/manganese dioxide system. Time of discharge is given in minutes. Lithium deinserts from the carbon ( $x$  decreases) and inserts into the manganese dioxide electrode on discharge.



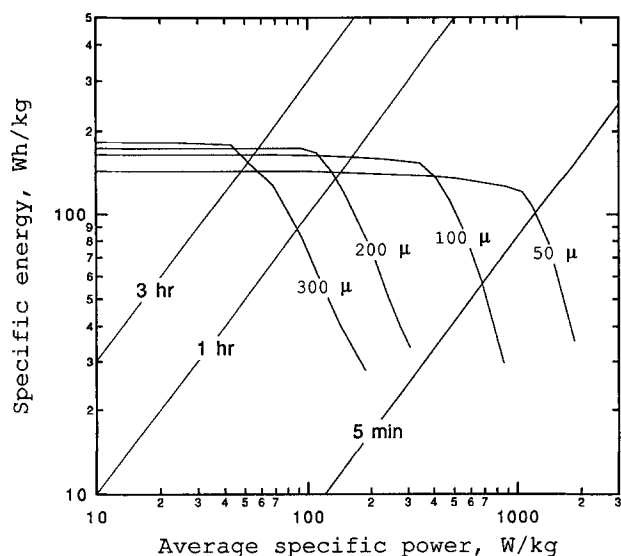


Fig. 8. Ragone plot for the manganese dioxide/carbon system. The thickness of the positive electrode is a parameter while the porosities and ratio of capacities of the two electrodes are kept constant. Other parameters used in the simulation are given in Tables I and II.

battery mass. This latter effect is only slightly apparent on Fig. 8 because the separator used here is thin, but it would be accentuated if the other battery components were included in calculating the mass. The slopes of the portion of the curves on Fig. 8 past the theoretical asymptote are all less than negative one.

Compare this figure with one given by Guyomard and Tarascon<sup>23</sup> (their Fig. 21) for the realizable specific energy and power of this system. Guyomard and Tarascon obtained their numbers by multiplying their experimental values (based on the mass of active material only) by a 33% hypothetical realization factor, a common rule of thumb. Our numbers are still only theoretical values, which account for the modeling predictions of polarization effects but do not account for additional battery masses, and hence they can be multiplied by some correction factor to account for additional battery masses. Comparing the figures, one immediately sees the similarity between results. For a particular thickness, such as 200  $\mu\text{m}$  (see Fig. 8), the predicted power at which the realizable energy begins to

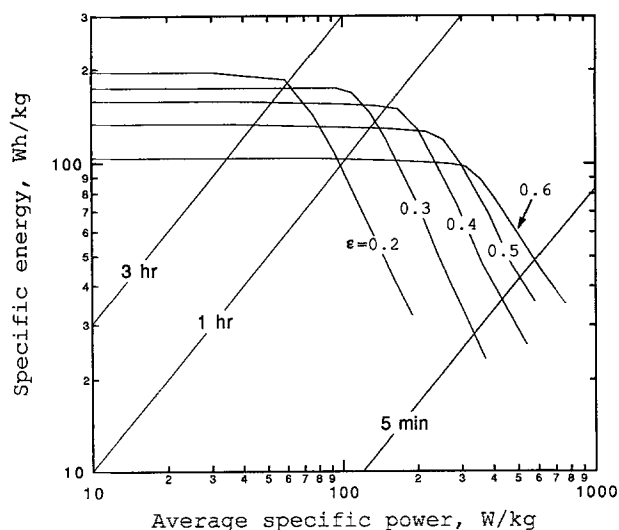


Fig. 9. Ragone plot for the manganese dioxide/carbon system. The porosity of the positive electrode (shown as a parameter) and that of the negative electrode vary while the thickness and ratio of capacities of the two electrodes are kept constant. Other parameters used in the simulation are given in Tables I and II.

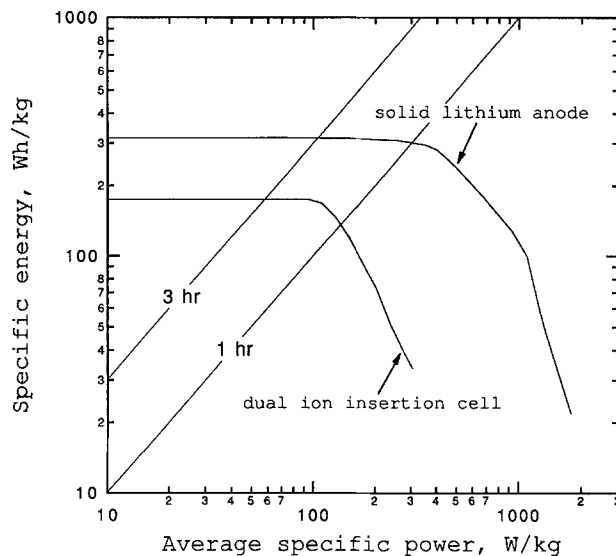


Fig. 10. Comparison of Ragone plots for the dual ion insertion and solid lithium electrode systems. The systems are identical except for the negative electrode. The solid lithium at full charge has four times the capacity required according to the stoichiometry. Other parameters used in the simulation are given in Tables I and II.

fall off from its theoretical asymptote is about three times the value obtained by Guyomard and Tarascon. It is necessary to interpolate when making these comparisons because different thicknesses were used in the two cases. However, the general trend of these plots is similar as the thickness is varied over the same range of values.

One scheme for optimizing the performance of the system is to generate curves such as Fig. 8 and 9 while varying different system parameters. If one had in mind minimum values of the specific energy and power for a particular application, ranges of parameters that satisfy these criteria could then be identified. In general, the optimization process is a complex one, as a multiple-parameter space must be explored to find the best compromise between attainable energy and power density.<sup>25</sup> Figure 9 demonstrates the effect of varying the porosities of both electrodes while holding their thicknesses constant and equal to the values in Table II. The ratio of capacities of the two electrodes is held constant, and the porosity of the filler is constant. This graph also exhibits a tradeoff of power and energy as the mass of the electrolyte increases. From this graph, one can pick an optimum porosity to use depending on the performance guidelines selected.

One last important comparison involves assessing the general effect of the additional carbon added to the negative electrode on the performance of the system. We have simulated the performance of the system given in Table I using a solid lithium anode instead of a carbon insertion material. The performance of these two systems is compared in Fig. 10. Two major reasons for using an insertion material instead of solid lithium are the growth of dendrites and film formation at the lithium surface. The film represents an irreversible loss of material and an additional ohmic drop, and decreases the reversibility of the surface on extended cycling. Films form on the carbon surface, but this condition does not seem to have as detrimental an effect on discharge and extended cycling capabilities. As our model does not allow for film formation or dendrites, the effects of these phenomena do not appear in the results given in Fig. 10. Figure 10 shows that the solid lithium system exhibits both better power and energy characteristics. The theoretical energy of the solid lithium system is ca. 70% higher than that of the dual lithium ion insertion system owing to a higher open-circuit potential and a lower total mass. The mass used for the solid lithium electrode corresponded to four times the stoichiometric amount required for full discharge, which is still signifi-

cantly less than the mass of the composite carbon electrode. For comparison, the mass per unit area of the foil electrode system is 0.077 g/cm<sup>2</sup>, while that of the dual insertion electrode cell is 0.108 g/cm<sup>2</sup>.

One conclusion that can be drawn from this comparison involves the maximum concentration of salt reached in the cell in either case. We have seen that a higher initial salt concentration improves the performance of the system, as long as the concentration of salt does not exceed the maximum concentration prescribed by a solubility limit. We find that a higher salt concentration is reached in the dual lithium ion insertion cell than when using a solid lithium electrode for a given discharge rate. For example, discharge rates above 5.0 mA/cm<sup>2</sup> cause the concentration to exceed the solubility limit of 2 · 10 mol/dm<sup>3</sup> in the dual insertion system simulated earlier. For the solid lithium system, the maximum concentration reached in the cell at this discharge rate is only 1.70 mol/dm<sup>3</sup>. Concentration depletion is less of a problem in the solid lithium cell, with the minimum concentration at the 5.0 mA/cm<sup>2</sup> rate being about 0.35 mol/dm<sup>3</sup>, instead of zero as in the dual insertion cell.

### Summary

A model is presented for predicting the discharge behavior of dual insertion cells. The model is general and can be used to simulate any cell utilizing two composite electrodes composed of a mixture of active insertion material, electrolyte, and inert conducting material. For example, we have demonstrated, here and in Ref. 17, the ability to treat Li and Li<sub>x</sub>C<sub>6</sub> negative electrodes, liquid and solid polymer electrolytes, and TiS<sub>2</sub> and Mn<sub>2</sub>O<sub>4</sub> positive electrodes. Other positive electrodes of interest include CoO<sub>2</sub>, V<sub>2</sub>O<sub>5</sub>, V<sub>6</sub>O<sub>13</sub>, and the lower plateau of Mn<sub>2</sub>O<sub>4</sub>. Transport properties, thermodynamic data, and cell specifications, integral to the simulation of these systems, are detailed. The utility of the model is presented for one particular system, the carbon/manganese dioxide cell with a solution of lithium perchlorate in propylene carbonate. Discharge curves are presented for various current densities, and the major process limiting high rates of discharge in this system is the increase in concentration overpotential because of depletion of the electrolyte. An analysis of the current distribution in these systems shows the importance of the rate of change of the open-circuit potential of the insertion material with the state of charge.

The optimization of these systems for a particular application has been discussed in terms of the attainable power and energy densities. The lithium ion dual insertion systems exhibit the large theoretical specific energy densities hoped for with lithium-based systems, although the energy necessarily is reduced from corresponding systems utilizing solid lithium anodes. The attainable power is also large, making thin cells ideally suited for high rate-of-discharge applications such as acceleration of electric vehicles. The energy and power densities quoted here represent simulated values, not accounting for losses due to extended cycling or additional battery mass. Yet even as such, the performance of these systems is promising, and it is likely that these cells will command an increasing amount of interest in the future.

### Acknowledgment

This work was supported by the Assistant Secretary for Conservation and Renewable Energy, Office of Transportation Technologies, Electric and Hybrid Propulsion Division of the U.S. Department of Energy under Contract No. DE-AC03-76SF00098.

Manuscript submitted May 10, 1993; revised manuscript received Oct. 6, 1993.

The University of California assisted in meeting the publication costs of this article.

### APPENDIX A

#### Transport Properties of the Electrolyte and Thermodynamic Data

Propylene carbonate, 1M LiClO<sub>4</sub>.—The concentration dependence of the conductivity was fit from available data of Gores and Barthel.<sup>23</sup> The diffusion coefficient of the salt<sup>15</sup>

( $D = 2.58 \times 10^{-6}$  cm<sup>2</sup>/s) and transference number of lithium<sup>26</sup> ( $t_+^0 = 0.2$ ) were taken to be constant, since reproducible data were not available. Activity coefficient data have not been reported.

**Electrode thermodynamic data.**—The open-circuit potential *vs.* state of charge for manganese dioxide<sup>27</sup> was fit to the function

$$U = 4.06279 + 0.0677504 \tanh [-21.8502y + 12.8268] - 0.105734 \left[ \frac{1}{(1.00167 - y)^{0.379571}} - 1.576 \right] - 0.045 \exp (-71.69y^8) + 0.01 \exp [-200(y - 0.19)] \quad [\text{A-1}]$$

where  $y$  is the amount of lithium inserted in Li <sub>$y$</sub> Mn<sub>2</sub>O<sub>4</sub>. This curve fit is given as Fig. A-1. Similarly, for the carbon electrode<sup>9</sup>

$$U = -0.132 + 1.41 \exp (-3.52x) \quad [\text{A-2}]$$

$x$  is the value defined by the formula Li <sub>$x$</sub> C<sub>6</sub>. Open-circuit-potential data were not available for this system, and the above function corresponds to the potential of carbon *vs.* lithium during a low current discharge. However, this is expected to resemble closely the open-circuit potential under these conditions (low discharge rate). This fit is presented as Fig. A-2.

### APPENDIX B

#### Superposition

Since the equations describing transport in the active cathode material are linear, contributions to the flux from a series of step changes in surface concentration can be superposed. This is an example of Duhamel's superposition integral<sup>21</sup>

$$\frac{\partial c_s}{\partial r}(R_s, t) = \int_0^t \frac{\partial c_s}{\partial t}(R_s, \zeta) \frac{\partial \bar{c}_s}{\partial r}(R_s, t - \zeta) d\zeta \quad [\text{B-1}]$$

where  $\bar{c}_s$  represents the solution to Eq. 10 for a unit step change in concentration at the surface. The above integral is calculated numerically using the method suggested by Wagner<sup>28</sup> and by Acrivos and Chambré.<sup>29</sup> Whence

$$\frac{\partial c_s}{\partial r}(R_s, t) = \sum_{k=0}^{n-2} \frac{(c_{s,k+1} - c_{s,k})}{\Delta t} A_{n-k} + \frac{(c_{s,n} - c_{s,n-1})}{\Delta t} A_1 \quad [\text{B-2}]$$

where

$$A_{n-k} = a[(n - k)\Delta t] - a[(n - k - 1)\Delta t] \quad [\text{B-3}]$$

and

$$a(t) = \int_0^t \frac{\partial \bar{c}_s}{\partial r}(R_s, \zeta) d\zeta \quad [\text{B-4}]$$

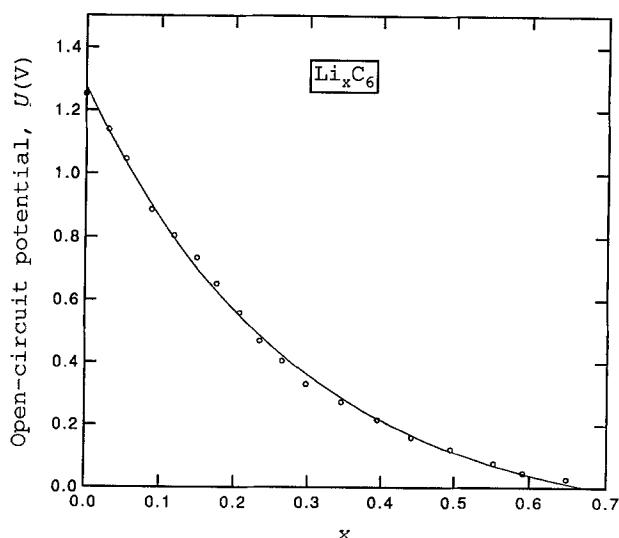


Fig. A-1. The open-circuit potential of manganese dioxide as a function of the state of charge relative to the potential of solid lithium at the same electrolyte concentration. Data reported by Ohzuku *et al.*<sup>26</sup>



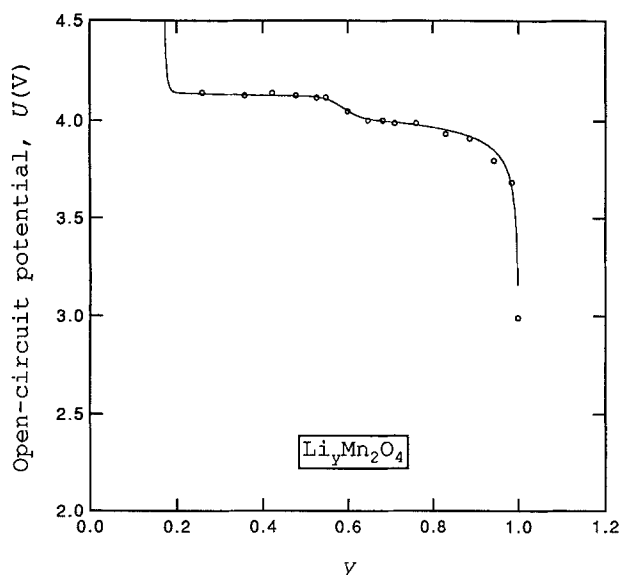


Fig. A-2. The open-circuit potential of carbon (petroleum coke) as a function of the state of charge relative to the potential of solid lithium at the same electrolyte concentration. Data reported by Fong *et al.*<sup>9</sup>

Two expressions for  $a(t)$  were developed with Laplace transforms: at long times

$$a(\tau) = \frac{2}{\pi^2} \sum_{n=1}^{\infty} \frac{1}{n^2} [1 - \exp(-n^2 \pi^2 \tau)] \quad [\text{B-5}]$$

and for short times

$$a(\tau) = -\tau + 2 \left( \frac{\tau}{\pi} \right)^{1/2} \left[ 1 + 2 \sum_{n=1}^{\infty} \exp\left(-\frac{n^2}{\tau}\right) - n \left( \frac{\pi}{\tau} \right)^{1/2} \operatorname{erfc}\left(\frac{n}{\sqrt{\tau}}\right) \right] \quad [\text{B-6}]$$

$\tau$  is dimensionless time;  $\tau = tD_s/R_s^2$ . These expressions are each uniformly valid; however, the latter expression converges much more quickly with fewer terms at very short times. The values of  $a(\tau)$  and  $A_{n-k}$  can be calculated separately and used whenever Eq. B-2 must be evaluated. This procedure, applicable for a constant diffusion coefficient, consequently is more efficient than solving for the two-dimensional transport directly.

#### LIST OF SYMBOLS

$a$	specific interfacial area, $\text{m}^2/\text{m}^3$
$c$	concentration of electrolyte, $\text{mol}/\text{dm}^3$
$c_i$	concentration of species $i$ , $\text{mol}/\text{dm}^3$
$D, D_s$	diffusion coefficient of electrolyte and of lithium in the solid matrix, $\text{cm}^2/\text{s}$
$f_A$	activity coefficient of salt
$F$	Faraday's constant, 96,487 C/eq
$i$	current density, $\text{mA}/\text{cm}^2$
$i_0$	exchange current density, $\text{mA}/\text{cm}^2$
$I$	superficial current density, $\text{mA}/\text{cm}^2$
$j_n$	pore-wall flux across interface, $\text{mol}/\text{m}^2 \cdot \text{s}$
$k$	reaction rate constant
$K_{ij}$	frictional coefficient, $\text{J} \cdot \text{s}/\text{m}^5$
$L$	thickness of cell, $\text{m}$
$n$	number of electrons transferred in electrode reaction
$N_i$	molar flux in $x$ direction of species $i$ , $\text{mol}/\text{m}^2 \cdot \text{s}$
$r$	radial distance in a particle of active material, $\text{m}$
$R$	universal gas constant, 8.3143 J/mol · K
$R_s$	radius of solid particles, $\text{m}$
$s_i$	stoichiometric coefficient of species $i$ in electrode reaction
$S_s, S_e$	dimensionless ratios defined in Eq. 19 and 20
$t$	time, $\text{s}$
$t_i^0$	transference number of species $i$

$T$	temperature, K
$U$	open-circuit potential, V
$v_i$	velocity of species $i$ , $\text{m}/\text{s}$
$V$	cell potential, V
$x$	distance from the negative electrode current collector, $\text{m}$
$x$	stoichiometric coefficient of lithium in carbon, defined by $\text{Li}_x\text{C}_6$
$\bar{x}$	dimensionless distance, defined by $\bar{x} = x/L$
$y$	stoichiometric coefficient of lithium in manganese dioxide, defined by $\text{Li}_y\text{Mn}_2\text{O}_4$
$z$	capacity ratio of positive to negative electrode
$z_i$	charge number of species $i$
$\alpha_a, \alpha_c$	transfer coefficients
$\delta_s$	thickness of separator, $\text{m}$
$\delta_+$	thickness of composite positive electrode, $\text{m}$
$\delta_-$	thickness of composite negative electrode, $\text{m}$
$\epsilon$	porosity
$\eta$	overpotential, V
$\kappa$	conductivity of electrolyte, $\text{S}/\text{cm}$
$\nu_+, \nu_-$	number of cations and anions into which a mole of electrolyte dissociates
$\rho$	density, $\text{g}/\text{cm}^3$
$\sigma$	conductivity of solid matrix, $\text{S}/\text{cm}$
$\tau$	dimensionless time
$\mu_i$	electrochemical potential of species $i$ , $\text{J}/\text{mol}$
$\Phi$	electrical potential, V

#### Subscripts

e	electrolyte
f	filler
ref	reference state
s	solid phase or separator
1	solid matrix
2	solution phase
t	concentration in intercalation material for $y = 1$
+	positive electrode
-	negative electrode

#### Superscripts

0	solvent, or initial condition
$\theta$	standard cell potential

#### REFERENCES

1. E. J. Cairns, *Interface*, **1**, 38 (1992).
2. *Lithium Batteries*, J.-P. Gabano, Editor, Academic Press, New York (1983).
3. *Sony's Lithium Manganese Rechargeable Battery (AA Size)*, p. 26, JEC Press, Inc., Cleveland, OH (1988).
4. *JEC Battery Newsletter*, No. 6, p. 15 (1988).
5. *Ibid.*, No. 3, p. 15 (1989).
6. D. Aurbach, M. L. Daroux, P. W. Faguy, and E. Yeager, *This Journal*, **135**, 1863 (1988).
7. R. Pollard and J. Newman, *ibid.*, **128**, 491 (1981).
8. K. M. Abraham, D. M. Pasquariello, and E. B. Willstaedt, *ibid.*, **137**, 743 (1990).
9. R. Fong, U. von Sacken, and J. R. Dahn, *ibid.*, **137**, 2009 (1990).
10. *Intercalation Chemistry*, M. S. Whittingham and A. J. Jacobson, Editors, Academic Press, New York (1982).
11. M. S. Whittingham, *This Journal*, **123**, 315 (1976).
12. J. Desilvestro and O. Haas, *ibid.*, **137**, 5C (1990).
13. M. Lazzari and B. Scrosati, *ibid.*, **127**, 773 (1980).
14. M. Armand, in *Materials for Advanced Batteries*, D. W. Murphy, J. Broodhead, and B. C. H. Steele, Editors, p. 145, Plenum Press, New York (1980).
15. B. Scrosati, *This Journal*, **139**, 2776 (1992).
16. K. West, T. Jacobsen, and S. Atlung, *ibid.*, **129**, 1480 (1982).
17. M. Doyle, T. F. Fuller, and J. Newman, *ibid.*, **140**, 1526 (1993).
18. J. Newman, *Electrochemical Systems*, Prentice-Hall, Englewood Cliffs, NJ (1991).
19. T. F. Fuller and J. Newman, *This Journal*, **139**, 1332 (1992).
20. R. E. Meredith and C. W. Tobias, in *Advances in Electrochemistry Electrochemical Engineering*, Vol. 2, p. 15, C. W. Tobias, Editor, Interscience (1962).
21. F. B. Hildebrand, *Advanced Calculus for Applications*, p. 463, Prentice-Hall Inc., Englewood Cliffs, NJ (1976).
22. R. Pollard and J. Newman, *Electrochim. Acta*, **25**, 315 (1980).
23. D. Guyomard and J. M. Tarascon, *This Journal*, **139**,

- 937 (1992).
24. H. J. Gores and J. Barthel, *J. Solution Chem.*, **9**, 939 (1980).
  25. G. G. Trost, V. Edwards, and J. S. Newman, in *Chemical Reaction and Reactor Engineering*, J. J. Carberry and A. Varma, Editors, Marcel Dekker, Inc., New York (1987).
  26. J. M. Sullivan, D. C. Hanson, and R. Keller, *This Journal*, **117**, 779 (1970).
  27. T. Ohzuku, M. Kitagawa, and T. Hirai, *ibid.*, **137**, 769 (1990).
  28. C. Wagner, *J. Math. Phys.*, **34**, 289 (1954).
  29. A. Acrivos and P. L. Chambré, *Ind. Eng. Chem.*, **49**, 1025 (1957).

# Electrochemical Synthesis of Composite Films of Manganese Dioxide and Polypyrrole and Their Properties as an Active Material in Lithium Secondary Batteries

Susumu Kuwabata, Akira Kishimoto, Takayoshi Tanaka, and Hiroshi Yoneyama\*

Department of Applied Chemistry, Faculty of Engineering, Osaka University, Yamada-oka 2-1, Suita, Osaka 565, Japan

## ABSTRACT

Composite films of polypyrrole and  $\beta$ -MnO<sub>2</sub> or lithiated MnO<sub>2</sub> (Li-MnO<sub>2</sub>) particles have been synthesized for use as cathode-active materials of rechargeable lithium batteries. The composite films were prepared by electrolysis of pyrrole dissolved in propylene carbonate solution in the presence of suspended MnO<sub>2</sub> particles. The maximum amount of the incorporation of MnO<sub>2</sub> was 50.2 and 40.6 weight percent for  $\beta$ -MnO<sub>2</sub> and Li-MnO<sub>2</sub>, respectively. It was found that both polypyrrole and the incorporated MnO<sub>2</sub> worked as the active material with one potential plateau in the charge-discharge test conducted in a mixed solution of propylene carbonate and dimethoxyethane in which LiClO<sub>4</sub> was dissolved. Furthermore, it was shown that polypyrrole worked as a conducting network for the incorporated MnO<sub>2</sub>. Though the utilization of the incorporated MnO<sub>2</sub> was not high ( $\beta$ -MnO<sub>2</sub> and Li-MnO<sub>2</sub> gave 0.23 and 0.57, respectively), the composite films prepared under optimal electrolysis conditions gave the specific energy density on volume basis of more than 150% of that obtained for a fully-utilized MnO<sub>2</sub>-free polypyrrole. Elemental analysis of the composite films revealed that electrolyte anions alone were involved in the redox reaction of polypyrrole of the composite films and Li<sup>+</sup> ions in the redox reaction of the incorporated MnO<sub>2</sub>.

Polypyrrole is one of the most popular conducting polymers, and its technological applications to a cathode-active material for rechargeable lithium batteries have widely been studied.<sup>1-7</sup> The redox reaction of polypyrrole is utilized as the charge-discharge reaction, and full utilization of polypyrrole in the redox reaction is essential for constructing a lithium secondary cell having a high energy density. The high utilization can be achieved by preparing highly porous polypyrrole films<sup>2d,3</sup> that allow easy insertion of electrolyte anions into the film in their oxidation and easy dissolution of the incorporated electrolyte anions into the electrolyte solution in their reduction. Even with the use of highly porous polypyrrole, however, the energy density on a volume basis is not so great, because the amount of electrolyte anions involved in the redox reaction of polypyrrole is limited to about 0.3 moles per unit mole of pyrrole ring.<sup>1,2</sup> This inferior property can be improved by incorporating electrochemically active anions into polypyrrole as a fixed dopant, as exemplified in our previous study with the use of anthraquinone sulfonate anion as the dopant.<sup>8</sup> We have also shown another approach in which anion-adsorbed manganese dioxide was used as the dopant.<sup>9</sup> Manganese dioxide is one of the promising materials as a cathode-active material for lithium secondary batteries.<sup>10-12</sup> However, since manganese dioxide possesses an extremely low conductivity, a conducting network is required to use it as the electroactive material. Usually carbon powder like acetylene black is mixed with manganese dioxide particles. If polypyrrole films containing MnO<sub>2</sub> particles, which will be denoted here as PPy/MnO<sub>2</sub>, are prepared, polypyrrole of the composite film must work not only as the conducting network for manganese dioxide but also as the active material. A previous communication demonstrated the validity of this view.<sup>9</sup> In this paper, we describe detailed investigations on preparation, character-

ization, and electrochemical properties of the PPy/MnO<sub>2</sub> composite films.

## Experimental

Pyrrole and 1,2-dimethoxyethane (DME) were used after distillation under atmospheric pressure. Propylene carbonate (PC) was purified by distillation under reduced pressure.  $\beta$ -MnO<sub>2</sub> powder was prepared by heating commercially available MnO<sub>2</sub> (Wako Pure Chemicals) at 300°C in air. Lithiated MnO<sub>2</sub>, which is denoted in this paper as Li-MnO<sub>2</sub>, was prepared by heating a mixture of LiOH · H<sub>2</sub>O and  $\beta$ -MnO<sub>2</sub> in a molar ratio of 3:7 at 375°C for 20 h in air.<sup>11</sup> The prepared  $\beta$ -MnO<sub>2</sub> and Li-MnO<sub>2</sub> had the specific surface area of 27.5 and 26.2 m<sup>2</sup> g<sup>-1</sup>, respectively, as determined by a high speed surface area analyzer (Shimadzu, Model 2205). The observation of the prepared MnO<sub>2</sub> powders with a Hitachi Model S-450 scanning electron microscope (SEM) revealed that the  $\beta$ -MnO<sub>2</sub> and the Li-MnO<sub>2</sub> particles had the same size distributions which ranged between 0.3 and 0.6  $\mu$ m, confirming the close similarity in the specific surface area of the two kinds of the manganese dioxide particles used in the present study.

The PPy/MnO<sub>2</sub> films were prepared by electrochemical polymerization of pyrrole in the presence of suspended MnO<sub>2</sub> particles using a glassy carbon plate as an anode. The glassy carbon plate was successively polished with 1.0 and 0.3  $\mu$ m alumina, followed by washing in an ultrasonic bath. The deposition bath of the PPy/MnO<sub>2</sub> film was propylene carbonate containing 0.1 mol dm<sup>-3</sup> pyrrole, 0.5 mmol dm<sup>-3</sup> tetraethylammonium chloride (TEACl) and various amounts of suspended MnO<sub>2</sub> except where specially noted. The polymerization was made at 0.1 mA cm<sup>-2</sup> under magnetically stirring the deposition bath in nitrogen atmosphere.

The PPy/MnO<sub>2</sub> was subjected to x-ray microanalysis before and after the charge-discharge tests using an energy dispersive Horiba EMAX 1800E analyzer connected to the

\* Electrochemical Society Active Member.